Nucleus softens during herpesvirus infection

Aapo Tervonen[1], Simon Leclerc[1], Visa Ruokolainen[1], Katie Tieu[2], Sébastien Lyonnais[3], Henri Niskanen[4], Jian-Hua Chen[5], Alka Gupta[1], Minna U Kaikkonen[4], Carolyn A Larabell[5], Delphine Muriaux[3,6], Salla Mattola[1], Daniel E Conway[2], Teemu O Ihalainen[7], Vesa Aho[1]*, Maija Vihinen-Ranta[1]*.

[1] Department of Biological and Environmental Science and Nanoscience Center, University of Jyvaskyla, Jyvaskyla, Finland.

[2]Department of Biomedical Engineering, The Ohio State University, Columbus, Ohio, USA.

[3]CEMIPAI, UAR3725, CNRS, Université de Montpellier, Montpellier, France.

[4]A.I. Virtanen Institute for Molecular Sciences, University of Eastern Finland, 70211 Kuopio, Finland.

[5]Molecular Biophysics and Integrated Bioimaging Division, Lawrence Berkeley National Laboratory, Berkeley, California, USA.

[6]UMR 9004 CNRS, IRIM (Institut de Recherche en Infectiologie de Montpellier), Université de Montpellier, Montpellier, France.

[7]BioMediTech, Faculty of Medicine and Health Technology, Tampere University, Tampere, Finland.

***Correspondence/equal contribution:** maija.vihinen-ranta@jyu.fi, vesa.p.aho@jyu.fi

Running title: Mechanical properties of the nucleus are remodeled in herpesvirus infection

Keywords: HSV-1, viral replication compartment, chromatin, nuclear lamina, LINC complex, nuclear stiffness

ABSTRACT

Mechanical properties of the nucleus are remodeled not only by extracellular forces transmitted to the nucleus but also by internal modifications, such as those induced by viral infections. During herpes simplex virus type 1 infection, the viral regulation of essential nuclear functions and growth of the nuclear viral replication compartments are known to reorganize nuclear structures. However, little is known about how this infection-induced nuclear deformation changes nuclear mechanobiology. Our analyses showed that the nucleus softens during the infection. To understand why this happens, we used microscopy and computational methods to study how the mechanical components of the nucleus are modified during the infection. We discovered that the viral replication compartment occupying the nuclear center has a low biomolecular density compared to the centrally located euchromatin in noninfected cells. The nuclear lamina was also modified such that in the infection the amount of lamin proteins increased and the nuclear envelope had more outward curved regions and moved less in infection compared to noninfected cells. The computational modeling of virus-induced changes in cellular forces showed that the most probable cause for the decreasing nuclear stiffness is the removal of lamina-associated domains or the decrease in outward forces, such as reduced intranuclear osmotic pressure and cytoskeletal pull. The simulations showed that an increase in the nuclear envelope tension can occur with a decrease in nuclear stiffness. Based on these findings, we propose a mechanical model that explains mechanistic coordination between the nuclear deformation in infection and decreased nuclear stiffness.

INTRODUCTION

Mechanical forces have an essential role in many cellular functions. Cells sense and react to external forces, which can lead to various responses such as changes in gene expression and cell differentiation[1–3]. Cells also generate intracellular forces, for example, to regulate cell shape and motion[4,5]. Intracellular forces are transmitted via cytoskeletal actin filaments and can be conveyed into the nucleus and further to the chromatin via the transmembrane proteins in the nuclear envelope (NE). In herpes simplex virus type 1 (HSV-1) infected cells, expansion of the viral replication compartment (VRC) and virus-induced manipulation of nuclear structure and functions leads to profound alterations of the nuclear milieu. However, little is known about how the infection remodels the mechanical properties of the nucleus.

The main mechanical components of the nucleus are the NE with its underlying nuclear lamina, the chromatin, and the filamentous nucleoskeleton[6,7]. The nuclear stiffness is often regulated by structural changes in the organization of the NE, chromatin, or both[8,9]. The nuclear lamina, a 14-nm-thick filamentous network associated with the inner nuclear membrane[10], mainly comprises intermediate filament lamins divided into A/C and B types[11]. The nuclear lamina reinforces the NE, connects to the cytoplasmic cytoskeleton via the linker of the nucleoskeleton and cytoskeleton (LINC) complex, and interacts with the lamina-associated domains (LADs) of the chromatin[12–14]. Reorganization of the lamina can lead to changes in the ability of the nucleus to resist deformations and large strains[15]. The rigidity of chromatin, another regulator of nuclear stiffness, is modulated by changes in its compaction state[9,15–18] and by the chromatin crosslinker HP1α[19]. DNA damage and the LAD connections also contribute to the mechanical strength of the nuclei[9,20]. Furthermore, osmotic pressure in the nucleus has been suggested to contribute to the nuclear mechanical response[21].

Viral infections can cause drastic changes in nuclear function and structure. HSV-1 infection leads to the formation and expansion of spherical and membraneless VRCs for viral DNA replication and progeny capsid assembly[22–24], which is accompanied by the reorganization of the host chromatin toward the nuclear periphery[25,26]. The VRC formation by the infection of HSV-1 and another herpesvirus, human cytomegalovirus, have some properties similar to liquid-liquid phase separation (LLPS), however, other compartmentalization mechanisms might also be included[27–29]. The substantial chromatin condensation toward the nuclear periphery regulates the diffusion of newly formed capsids through the chromatin to the NE[30–33], where the first step of nuclear egress, viral primary envelopment through the inner nuclear membrane, is assisted by the viral nuclear egress complex and disintegration of the nuclear lamina[34–36]. The activity of viral UL34 and US3 proteins leads to the local disintegration of lamin A/C and lamin B[37,38].

In this study, we analyze HSV-1 infection-induced changes in the nuclear biomechanics in host cells using various experimental methods, including fluorescence microscopy, volume electron microscopy (EM), cryo-soft X-ray tomography (SXT), and atomic force microscopy (AFM), as well as using computational modeling. Our data shows that the nuclei become softer upon the progression of infection as the nuclear structure undergoes profound changes and the nuclear lamina is modified. Modeling suggests that besides these changes, osmotic pressure and cytoskeletal pull to the nucleus might contribute to the softening.

RESULTS

Nuclear stiffness decreases as the infection proceeds

To analyze how HSV-1 infection alters nuclear elasticity, we measured the mechanical response of Vero cell nuclei using AFM[39]. The AFM analysis includes indentation of the nucleus using a cantilever with a spherical tip. The measurement of the bending of the cantilever with a known spring constant provides the force applied to the nucleus (Figs. 1a and 1b, Supplementary Movie 1), which allows quantification of the elastic modulus of the nucleus, i.e., nuclear stiffness[40,41]. The measurement was conducted in intact cells, so even though almost all the volume under the tip consists of the nucleus, thin layers of cytoplasm remain above and below the nucleus.

There was a large variation in the stiffness of noninfected cell nuclei with measured values between 500 and 3,000 Pa. Compared to noninfected cells, the mean stiffness during the infection was lower at 4 hours post infection (hpi) and kept decreasing until 8 hpi, when Young's modulus was only about one fourth of the noninfected cell value (Fig. 1c). Finally, after this there was a minor recovery at 10 hpi.

Our finding shows that the progression of HSV-1 infection softens the nucleus. To understand this phenomenon, we next studied how the mechanical components of the nucleus, such as the chromatin or nuclear lamina, are modified by the infection.

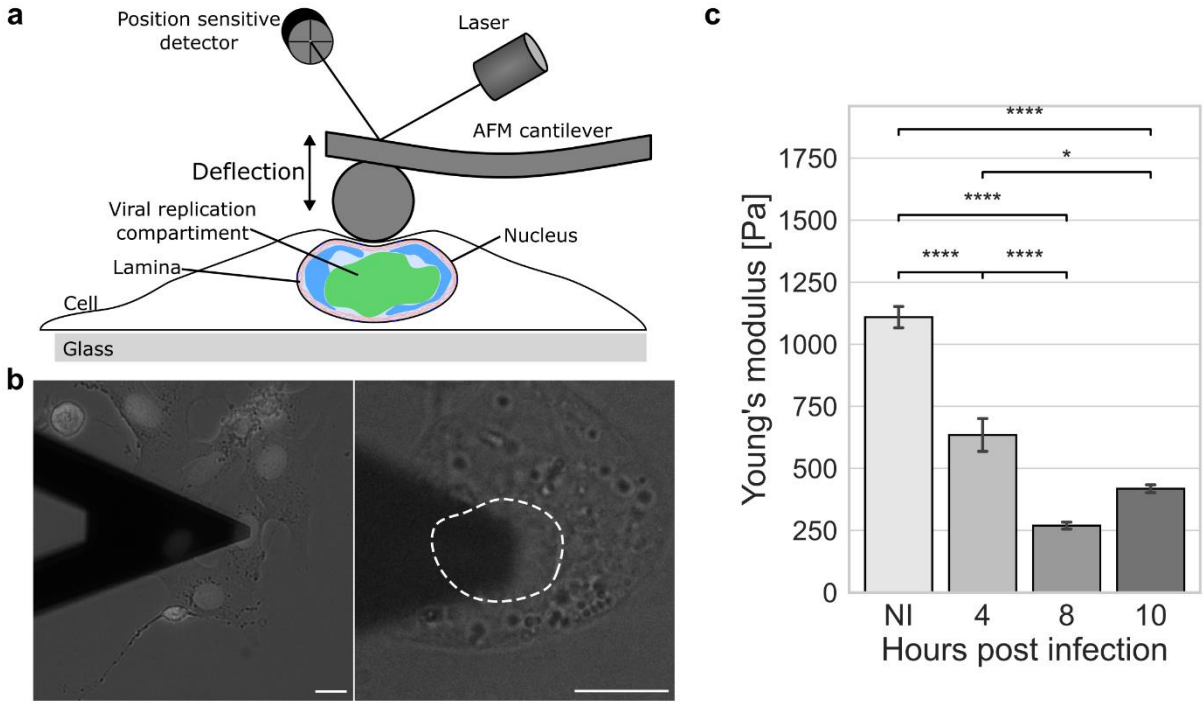

Figure 1. Nuclear stiffness decreases during the progression of infection.
(**a**) Schematic side view of an atomic force microscope (AFM) cantilever with a colloidal probe over a nuclear region of the cell. (**b**) Brightfield microscopy images of the infected cell underneath the AFM cantilever at 8 hpi. The nuclear periphery is demarcated with a dotted white line. Infected Vero cells were identified with the presence of ICP4 by epifluorescence. See also Supplementary Movie 1. (**c**) AFM analysis of nuclear stiffness was performed on noninfected and HSV-1 ICP4-EYFP infected cells at 4, 8, and 10 hpi (n=255, 50, 129, and 129, respectively). Ten successive force curve measurements were taken on each cell, and the Hertz model was used to calculate the average Young's modulus. Statistical significance was determined using Tukey's test. The significance values shown are denoted as **** ($p<0.0001$) and * ($p<0.05$). Nonsignificant differences ($p \geq 0.05$) are not labeled.

Molecular density of the nuclear center decreases in the infection

In the lytic HSV-1 infection, the nuclear import of the viral genomes is followed by the emergence of distinct punctate VRCs at early infection (1–5 hpi)[42]. Later in infection (8–12 hpi), the growth and fusion of the VRC foci result in the formation of an enlarged VRC, marginalization of host cell chromatin next to the nuclear envelope, and growth of the nuclear volume[25,26,43].

SXT imaging and analysis of infected mouse embryonic fibroblast (MEF) cells at 8 hpi showed that biomolecular density (quantified by linear absorption coefficient, LAC) in the central areas of the nucleus, occupied by the VRC (Figs. 2a and 2b, Supplementary Movie 2), was lower

than that in the euchromatin areas of the noninfected cells (Fig. 2c). Notably, the density of the perinuclear chromatin of infected cells remained similar to the density of the heterochromatin of noninfected cells (Fig. 2d).

To study further the distribution and organization of chromatin in the nucleoplasm of MEF cells, we used focused ion-beam scanning electron microscopy (FIB-SEM) together with ChromEM chromatin labeling method[44]. This approach confirmed the presence of dense chromatin close to the NE in infected cells at 8 hpi (Fig. 2e). Notably, finger-like protrusions of dense chromatin towards the center of the nucleus were less pronounced in infected cells. However, small dense chromatin aggregates were still detected in the central area of the nucleus where the VRC and viral capsid were located (Figs. 2f and 2g, Supplementary Movie 3). This can be cellular chromatin remaining in the VRC region or replicated viral genomes[45]. The ChromEM labeling can detect viral DNA, as shown by the intense labeling of full (DNA-containing) capsids (Supplementary Fig. S1).

Altogether, the enlarged low-density region emerging during the infection had a lower density than the central parts of noninfected cells, and the density decreased as the infection proceeded, which might have implications on the nuclear softness during the infection. The marginalized chromatin of the infected cell was not denser than the control cell heterochromatin.

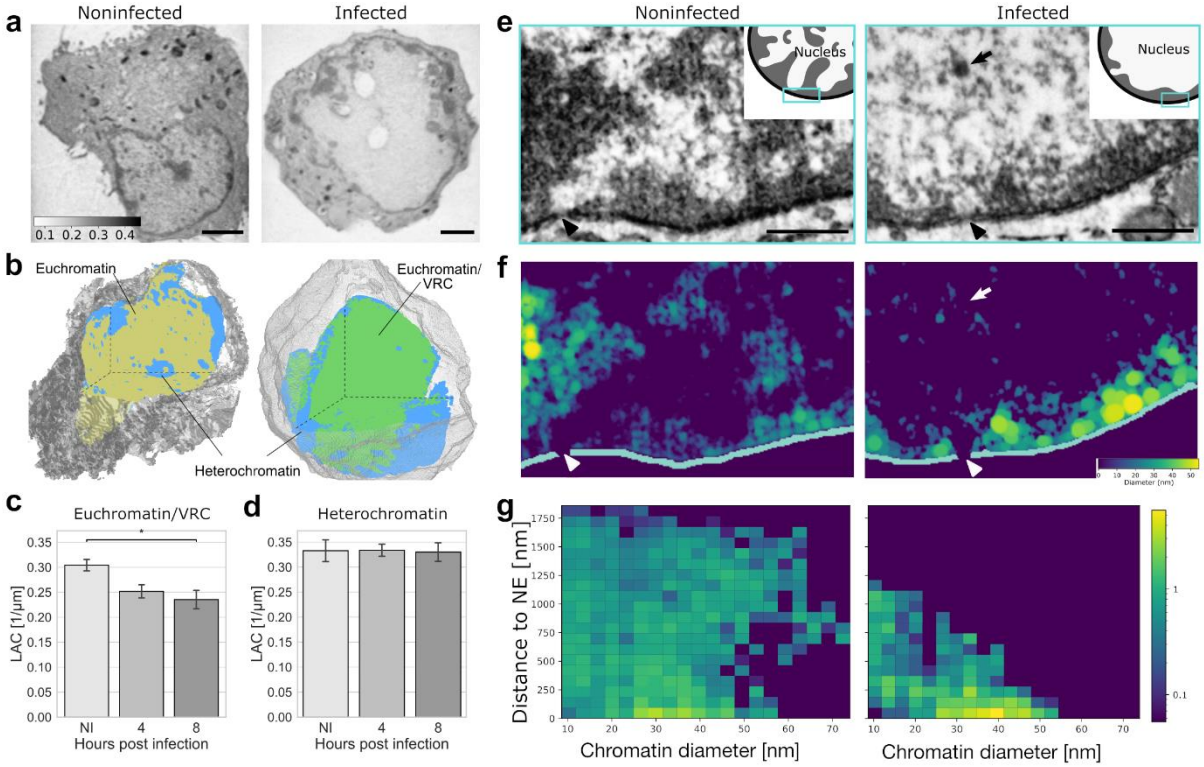

Figure 2. The enlarged viral replication compartment has a low biomolecular density.
(**a**) Cryo-soft X-ray (SXT) tomography ortho-slices of noninfected (NI) and infected mouse embryonic fibroblast (MEF) cells at 8 hpi. (**b**) Molecular densities are presented in a continuous grey scale representing linear absorption coefficient values ranging from 0.1 to 0.4 μm^{-1} (bar). Scale bars, 2 µm. (**b**) Cross-sections of 3D SXT reconstructions of noninfected and infected cells. The high-density region (heterochromatin) is shown in blue, the low-density region (euchromatin) in yellow, the viral replication compartment (VRC/euchromatin) area in green, and the cytoplasm in grey. See also Supplementary Movie 2. Quantitative analysis of linear absorption coefficient (LAC) of the (**c**) low-density and (**d**) high-density region in noninfected and infected cells 4 and 8 hpi (n=6). (**e**) Representative cross-sections of focused ion beam scanning electron microscopy (FIB-SEM) images of noninfected and infected MEF cells at 8 hpi. The viral capsid (arrows) and nuclear pore complexes (arrowheads) are shown. Scale bars, 0.5 µm. See also Supplementary Movie 3. (**f**) Reconstruction of chromatin density and (**g**) thickness of chromatin fibers as a function of the distance from the nuclear envelope in noninfected and infected cells. The color bar indicates the high and low chromatin densities (yellow-green) and high and low thickness (yellow-blue). Statistical significance was determined using Tukey's test. The significance values shown are denoted as * ($p<0.05$). Nonsignificant differences ($p \geq 0.05$) are not labeled.

The nuclear expansion is regulated by lamins

The progression of HSV-1 infection leads to the growth of the nuclear volume[26]. Here, we studied how the amount of A-type lamins and the presence of truncated and farnesylated lamin A protein, progerin[46], affects the nuclear size of Vero cells. Confocal microscopy showed that the progression of infection and overexpression of lamin A/C increased nuclear volume, whereas the presence of progerin reduced it (Figs. 3a and 3b). Lamin A/C was localized to the nuclear envelope, but progerin mutation caused it to localize additionally into the cytoplasm in

noninfected and infected cells (Fig. 3a). Both the excess of lamin A/C and progerin resulted in a more scattered distribution of ICP4 at 8 and 12 hpi in comparison to the solid VRCs seen in the wild-type cells. The lamin A/C overexpression and progerin also led to more uniform chromatin localization compared to marginalization close to the NE in the infected cells (Fig. 3a). The quantitative data analysis confirmed that in the cells with endogenous expression of lamin A/C, the progression of infection to 12 hpi induced enlargement of the nucleus compared to noninfected cells (Fig. 3b). In lamin A/C overexpressing cells, the infection induced a larger nuclear volume increase when compared to the cells with endogenous levels of lamin A/C: the nuclear volume change from noninfected cells to 12 hpi was 1.33-fold in lamin A/C overexpressing cells compared to 1.24-fold increase in wild-type cells. In progerin-expressing cells, the nuclear volume decreased as the infection proceeded. The nuclear height remained relatively unchanged in all cases even in the presence of progerin (Fig. 3c). To summarize, the progression of infection led to an increase in the nuclear volume and the expansion was enhanced by lamin A/C overexpression and inhibited by progerin.

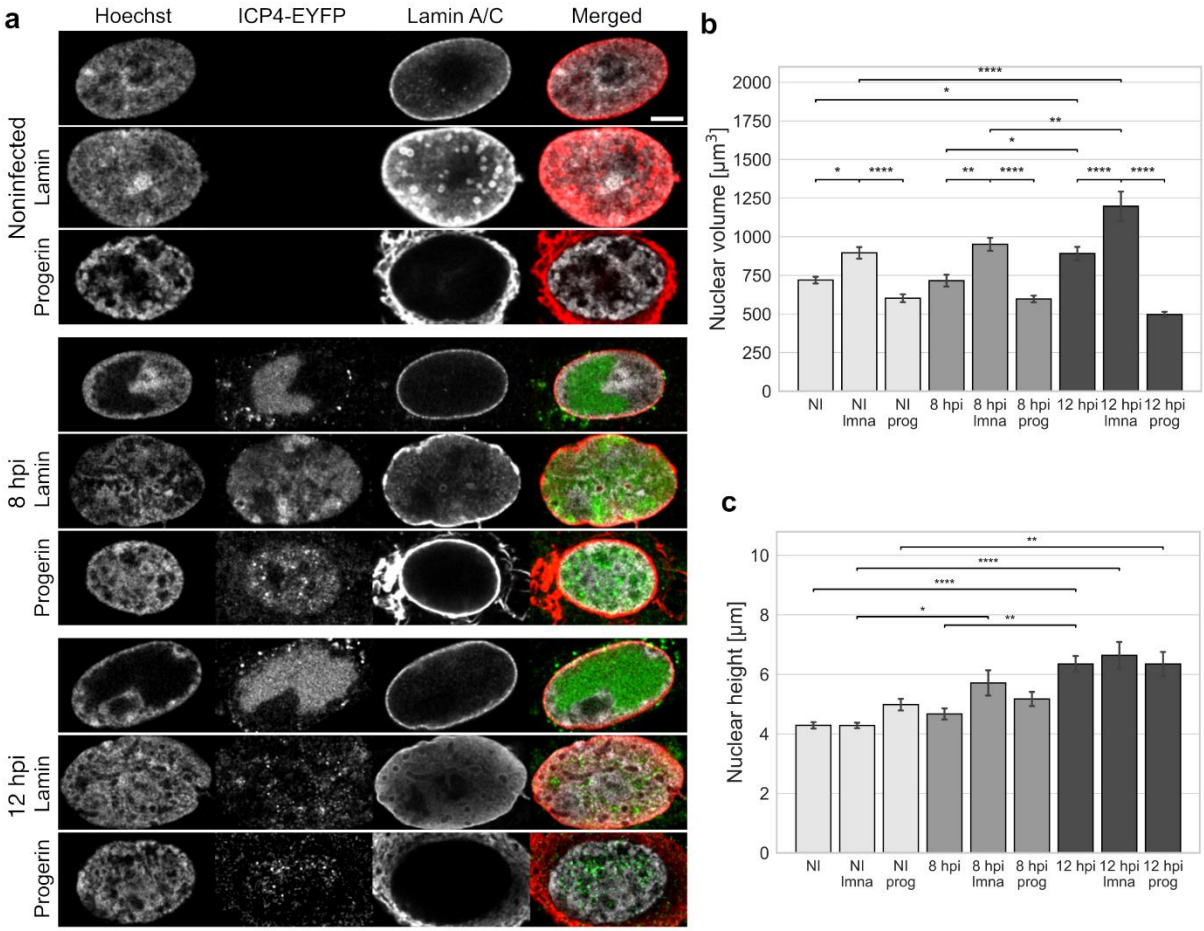

Figure 3. Overexpression of lamin A enhances nuclear growth.
(**a**) Representative confocal images of noninfected and HSV-1 EYFP-ICP4-infected Vero cells at 8 and 12 hpi are shown. Vero cells overexpressing lamin A (lmna) and expressing progerin (prog), a truncated version of lamin A, are also shown. Lamin A/C was labeled with lamin A/C antibody (red), EYFP-ICP4 (green) shows the localization of the VRC, and the chromatin was labeled with Hoechst 33342 (grey). Quantitative analysis of (**b**) the volume and (**c**) the height of the nucleus in noninfected (NI) and infected cells. Statistical significance was determined using Tukey's test. The significance values shown are denoted as **** ($p < 0.0001$), ** ($p < 0.01$), or * ($p < 0.05$). Only values of the same time point or the same treatment were statistically compared. Nonsignificant differences ($p \geq 0.05$) are not labeled.

The lamin motion decreases and the nuclear membrane tension increases during the infection

The mobility of lamins has a role in regulating nuclear stiffness[47]. We used lamin A/C chromobody to assess differences in the nuclear lamina properties and motion in living, noninfected and infected, Vero cells[48]. We hypothesized that the mechanical properties of the nuclear envelope are connected to the shape and mobility of the lamina, and the internal pressure increase (or decrease) would cause the nucleus to bulge (or wrinkle), respectively. To analyze the lamina shape, it was segmented, skeletonized, and discretized. Finally, local

regions of positive and negative curvature were quantified (Fig. 4a). The proportion of negative curvature regions was smallest at 8 hpi (Fig. 4b), but the change was not statistically significant. Next, the extent of lamina fluctuations was analyzed by taking the maximum intensity projection of the segmented and skeletonized lamina over the time series and calculating its area (Fig. 4c). The motion of the nuclear lamina, quantified as the area covered by the lamina skeleton during the time series and normalized by the length of the lamina, was significantly smaller at 8 hpi than in noninfected cells (Fig. 4d). This shows that the motion of the lamina decreases in infection, indicating higher tension or reduced mechanical dynamics of the lamina. Finally, the nuclear membrane tension was measured by ER Flipper-TR probe and fluorescence lifetime imaging microscopy (FLIM)[49]. In line with the nuclear lamina motion analysis, changes in the fluorescence lifetime indicated an increase in the tension near the NE at 12 hpi in comparison to noninfected and infected cells at 8 hpi (Figs. 4e and 4f).

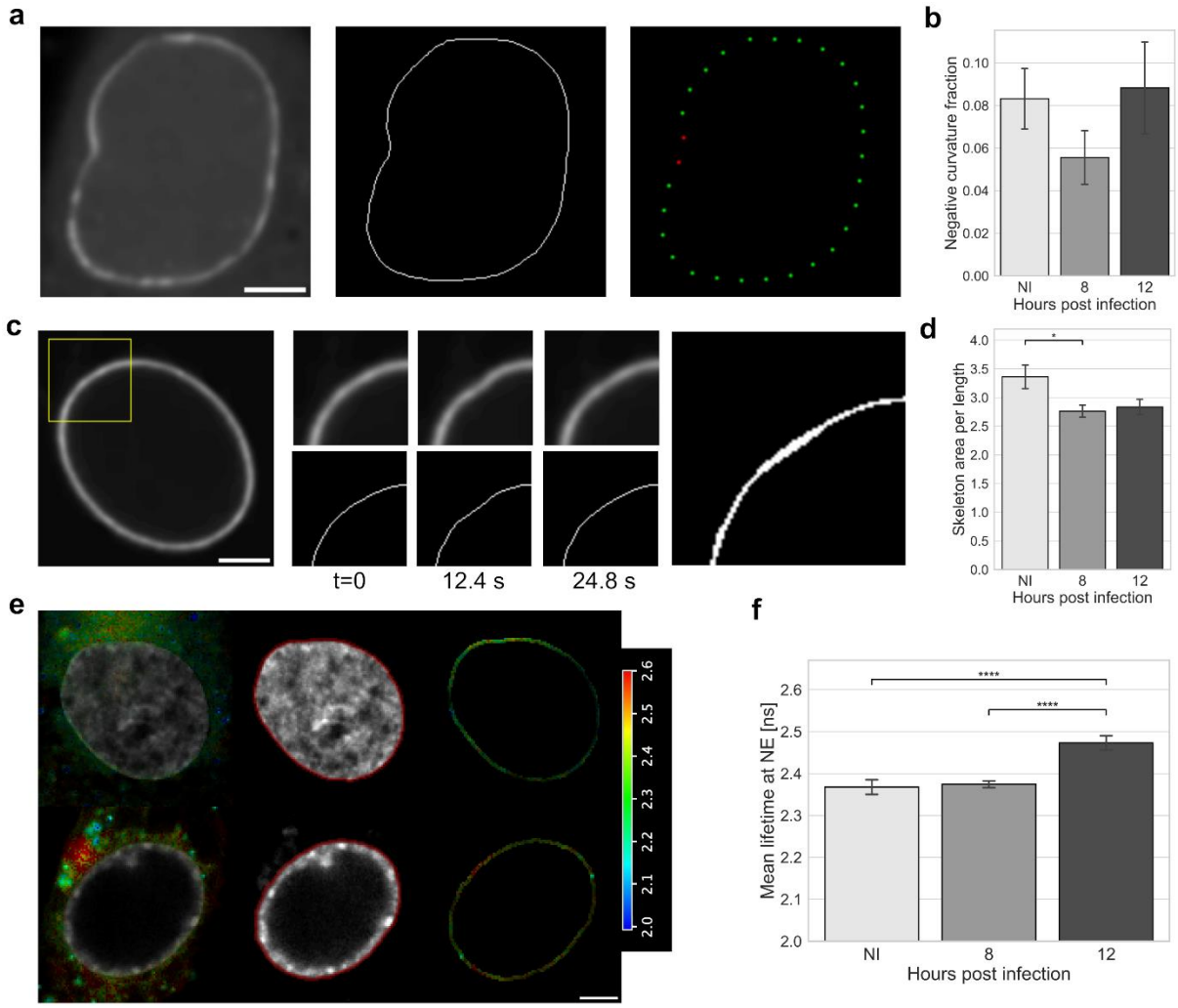

Figure 4. The motion of nuclear lamina decreases in infection.
(**a**) Nuclear lamina labeled by lamin A chromobody, skeletonization of the lamina, and discretized lamina points showing regions of positive (green) and negative curvature (red) in infected Vero cells at 8 hpi. (**b**) The fraction of negative curvature points of the whole lamina. **(c)** A zoom-in of the nuclear lamina, showing its motion and maximum intensity projection of the skeleton during 24.8 s. Scale bars, 5 µm. (**d**) Nuclear lamina mobility, measured as the area covered by the skeleton during one minute for noninfected cells and cells imaged 8 and 12 hpi (n=19, 22, and 17, respectively). (**e**) Nuclear envelope (NE) tension analysis by fluorescence lifetime imaging microscopy (FLIM) of noninfected and HSV-1 17+ wild-type virus-infected Vero cells at 12 hpi using fluorescence lifetime reporting membrane tension probe ER Flipper-TR. A fast FLIM image presented in a continuous pseudocolor scale representing average photon arrival times in each pixel ranging from 2.0 to 2.6 ns (color bar). Representative cells with average lifetime distribution, segmented NE (red) around the Hoechst signal (grey), and average lifetime at the NE region are shown. Scale bar, 10 µm. (**f**) The longer lifetime component of the ER Flipper probe describes the membrane tension in noninfected and infected cells at 8 and 12 hpi (n=51, 58, and 59, respectively). Statistical significance was determined using Tukey's test. The significance values shown are denoted as *($p<0.05$) or **** ($p<0.0001$). Nonsignificant differences ($p \geq 0.05$) are not labeled.

The amount of lamins increases late in infection despite their downregulation

The nuclear lamina is one of the major determinants of the mechanical behavior of nuclei, and thus, to explore the transcriptional activity of lamina-associated proteins during infection, we employed a Global Run-On sequencing (GRO-Seq) analysis in Vero cells. The gene ontology

analysis (GO) of GRO-Seq data according to the PANTHER classification system for the GO Biological process (http://www.pantherdb.org) identified 3 main categories: protein localization to the NE (GO:0090435), nuclear migration (GO:0007097), and NE organization (GO:0006998) (Fig. 5 a,b Supplementary Table 1). At 4 hpi, the genes encoding lamins A/C and B2 were upregulated, whereas at 8 hpi genes encoding both lamin B1 and B2 were downregulated. Notably, transcription of SUN2, one of the essential proteins of the LINC complex, the key regulator of nucleus-cytoskeleton connections[50], was strongly downregulated at 8 hpi. The zinc metallopeptidase STE24 (ZMPSTE24), a protein needed during the preprocessing of lamin A[51], was upregulated both at 4 and 8 hpi. This protein has a strong antiviral activity inhibiting the replication of many enveloped DNA and RNA viruses[52,53]. The clustering of genes (https://string-db.org/) (Fig. 5c, Supplementary Table 1) confirmed an interaction between unregulated SUN2 and lamin A/C, B2, and downregulated B1 at 4 hpi. In addition, lamin A/C interacted with the upregulated Torsin 1A interacting protein 1 (TOR1AIP1, also known as LAP1), a protein involved in the connection between the nuclear membrane and the nuclear lamina[54–56]. At 8 hpi, TOR1AIP1 transcription remained upregulated, but SUN2 became downregulated. This could lead to decreased interaction between SUN2 and LINC complex components, nesprin family proteins, encoded by SYNE 1–4 genes[57]. Confocal imaging of lamin A/C and B showed that they were distributed to the nuclear rim in noninfected and infected Vero cells (Fig. 5d). In infected cells, the total nuclear intensity of lamins, especially lamin A/C, increased at 8 hpi compared to noninfected cells. The total amount of lamins was highest at 12 hpi, because lamin A/C remained unchanged and lamin B increased from 8 to 12 hpi (Fig. 5e). The amount of lamins analyzed near the nuclear envelope followed a similar pattern as the amount in the whole nucleus (Supplementary Fig. S2). Since the transcription of lamin and lamin-associated proteins declined at 8 hpi, this most likely decreases the amounts of lamins at later stages of the infection. Altogether, our findings

show that transcription of key regulators of the cytoskeleton–nucleus force transmission, B-type lamins, and LINC complex protein SUN2, were downregulated at 8 hpi. However, this did not reduce the amount of lamin proteins at 12 hpi.

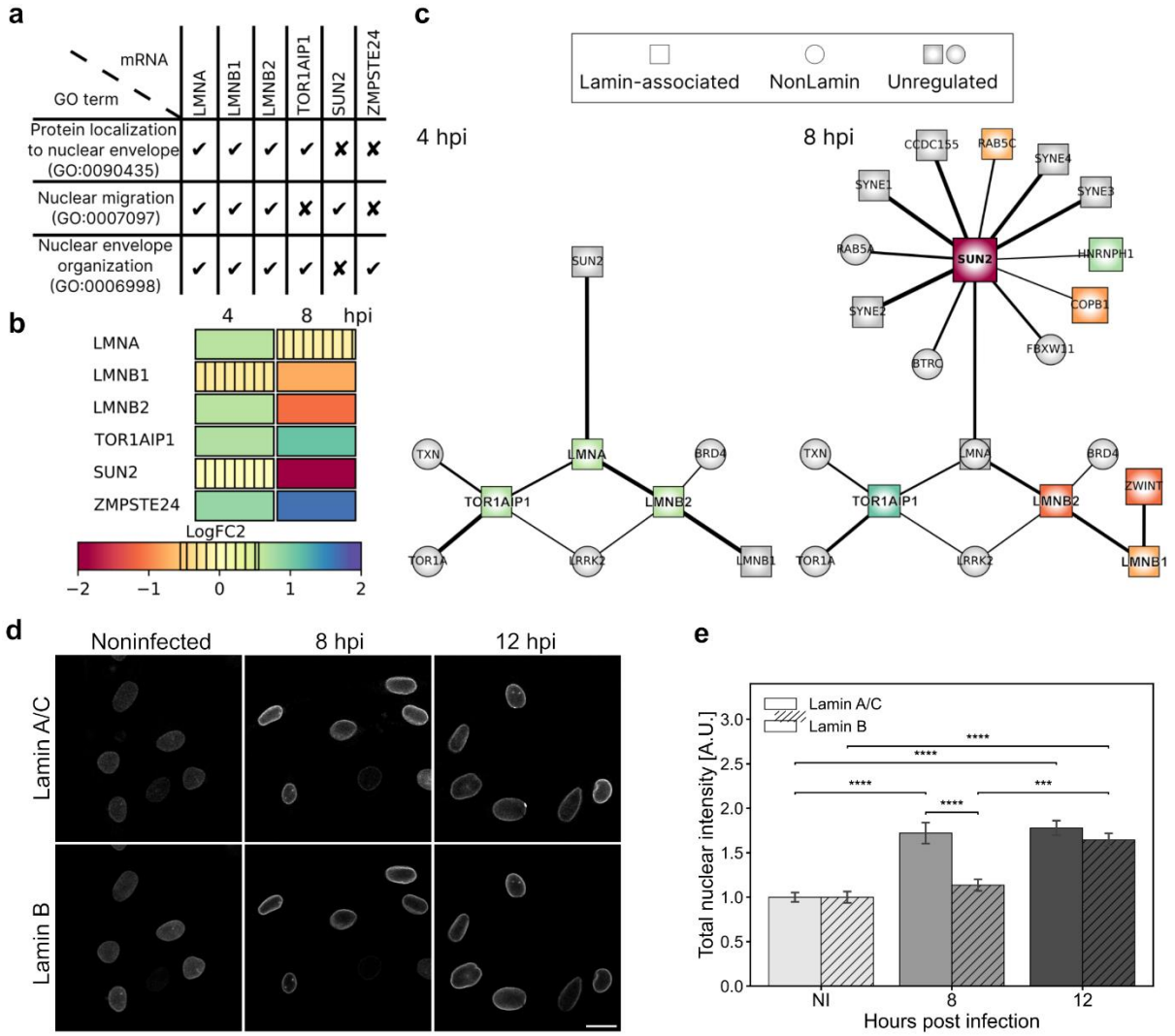

Figure 5. The amount of lamins increases in infection.
Global run-on sequencing (GRO-seq) analysis of nascent RNA levels of nuclear lamins and lamin-associated proteins in infected Vero cells at 4 and 8 hpi. (**a**) GO term classification for lamin-associated processes and (**b**) regulation of proteins. The color bar indicates upregulation (green-blue) or downregulation (orange-red), and low change of gene transcription (vertical stripes). (**c**) The genes encoding for lamins and lamin-associated proteins (square-shaped nodes), as well as cellular interactor proteins not associated with lamins (round-shaped nodes), are shown. The upregulated (green-blue) or downregulated (red-orange) transcripts in response to the infection are visible together with unregulated interacting transcripts (grey). The node size correlates with a logarithmic fold change (logFC) of regulation, and the thickness of black lines between nodes is proportional to the interaction in the STRING database (https://string-db.org/). (**d**) Distribution of lamin A/C and B in noninfected and HSV-1 ICP4-EYFP-infected Vero cells at 8 and 12 hpi. (**e**) Normalized fluorescence intensity of lamin A/C and B in the nuclei of noninfected and infected cells at 8 and 12 hpi (n=74, 62, and 54, respectively). Statistical significance was determined using Tukey's test. The significance values shown are denoted as **** ($p<0.0001$) or *** ($p<0.001$). Nonsignificant differences ($p \geq 0.05$) are not labeled.

Computational modeling explains the nuclear softening

Our experimental data indicated that the amount of lamin proteins increases, the nuclear lamina becomes less mobile, and its outward curvature increases in HSV-1-infected cells. These changes suggest that the nuclear envelope becomes less elastic during the infection. However, AFM indentation measurement suggested that nucleus stiffness reduces during the infection. To understand the seemingly contradicting mechanical changes of the nucleus in HSV-1 infected cells, we built a computational model of the nucleus to simulate the possible scenarios leading to the observed changes. The model consisted of the two components that determine the main mechanical properties of the nucleus, the NE, considered to include the nuclear lamina, and the chromatin. Furthermore, the connections between the two, LADs, and transient crosslinks within the chromatin were included in the model. The NE was modeled as a thin 3D triangulated shell, whereas the chromatin was represented by a polymer model. Additionally, an outward force, describing a combination of outward osmotic pressure and cytoskeletal forces on the NE, was included. Finally, to describe the VRC, another shell, similar to the NE, was added inside the nucleus and grown to an appropriate size to marginalize the chromatin towards the periphery (Fig. 6a, Supplementary Movie 4). Model parameters for the noninfected nucleus were taken either from the literature or fitted by replicating the AFM experiments (Supplementary Movie 5).

To study the nuclear mechanics during HSV-1 infection, various model parameters were iteratively adjusted for observation of their impact on the simulated AFM results. Based on the observed low molecular density (Figs. 1a-c), we hypothesized that the VRC is very soft and disregarded its role in the infected cell AFM simulations. Additionally, we postulated that most of the changes seen in Young's modulus were due to the morphological and structural alterations of the nucleus, rather than the cytoplasm. First, we examined the effect of the nuclear

volume and height change on the simulated AFM results while keeping everything else constant (Fig. 6b). While there was no change in the simulated Young's moduli between the noninfected and 8 hpi similar-sized nuclei, the increase in the nuclear size at 12 hpi led to a significant increase in the simulated stiffness compared to the noninfected nuclei. Furthermore, since the amount of lamin approximately doubled at late infection (Supplementary Fig. S2), we simulated the infected cases with doubled values for the lamina mechanical parameters. These changes led to further increased stiffness compared to the respective simulations with the base lamina parameters. Next, we simulated the effect of chromatin marginalization on the simulated Young's moduli and found no significant effect (Fig. 6c). Finally, we investigated the importance of lamina-chromatin tethering by simulating the 8 hpi nuclei with and without LADs and found that their omission significantly reduced Young's modulus (Fig. 6d). However, this decrease in stiffness was quite minor compared to the experimentally observed change between noninfected and 8 hpi nuclei. Therefore, since these changes in the nucleus could not fully explain the experimentally observed reduction in nuclear stiffness, other mechanical changes must occur in the nucleus during HSV-1 infection.

To understand the changes in nuclear mechanics that could result in the reduction in Young's modulus, we focused on two key changes: decreased outward force and lamina disintegration (Figs. 6e and 6f, Supplementary Fig. S3). The first change includes either the decrease in osmotic pressure difference between the cytosol and the nucleus, or the decrease in cytoskeletal force on the nucleus via the LINC complexes. Lamina disintegration, a phenomenon observed during HSV-1 infection, was described to result in a reduction in the mechanical strength of a given percentage of connections in the lamina without changing the number of LADs. In general, the decrease in the outward forces had the most significant effect, as shown by the reduction of the simulated Young's moduli. Finally, lamina disintegration was generally

insignificant when the outward forces were high but became more important at lower strengths of the outward forces. Thus, our computational data suggested that the outward force, including osmotic pressure and cytoskeletal forces, had the most prominent effect on the nuclear stiffness. Analysis of morphological changes revealed that the cell contact area occupied by the actin-labeled cells was reduced in infection (Supplementary Fig. S4), which suggests that the decrease of the outward forces by reduced actin cytoskeleton pull might be a relevant situation in the infection.

Next, we analyzed the NE membrane tension after decreased outward forces and disintegration of the lamin network. We found that tension in the nuclear membrane is affected by both lamina disintegration and the decrease in outward forces (Fig. 6g, Supplementary Fig. S3). Lamina disintegration led to a significant increase in the nuclear membrane tension, while a reduction of outward forces decreased the tension significantly. The increase in membrane tension during lamina disintegration can be explained by the larger share of the outward forces falling on the membrane rather than the lamina. Furthermore, we compared the distribution of lamina tension in the NE as the lamina was disintegrated (Fig. 6h and 6i). There were more local high-tension spots on the top surface of the nucleus as the lamina disintegrated. In all cases, the tension was higher on the sides of the nucleus (Fig. 6h), which is explained by the fact that there is no actin cap pushing against the nuclear outward forces in these regions. The simulation results thus indicate that a decrease in nuclear stiffness can occur with increases in the nuclear membrane and local lamina tension.

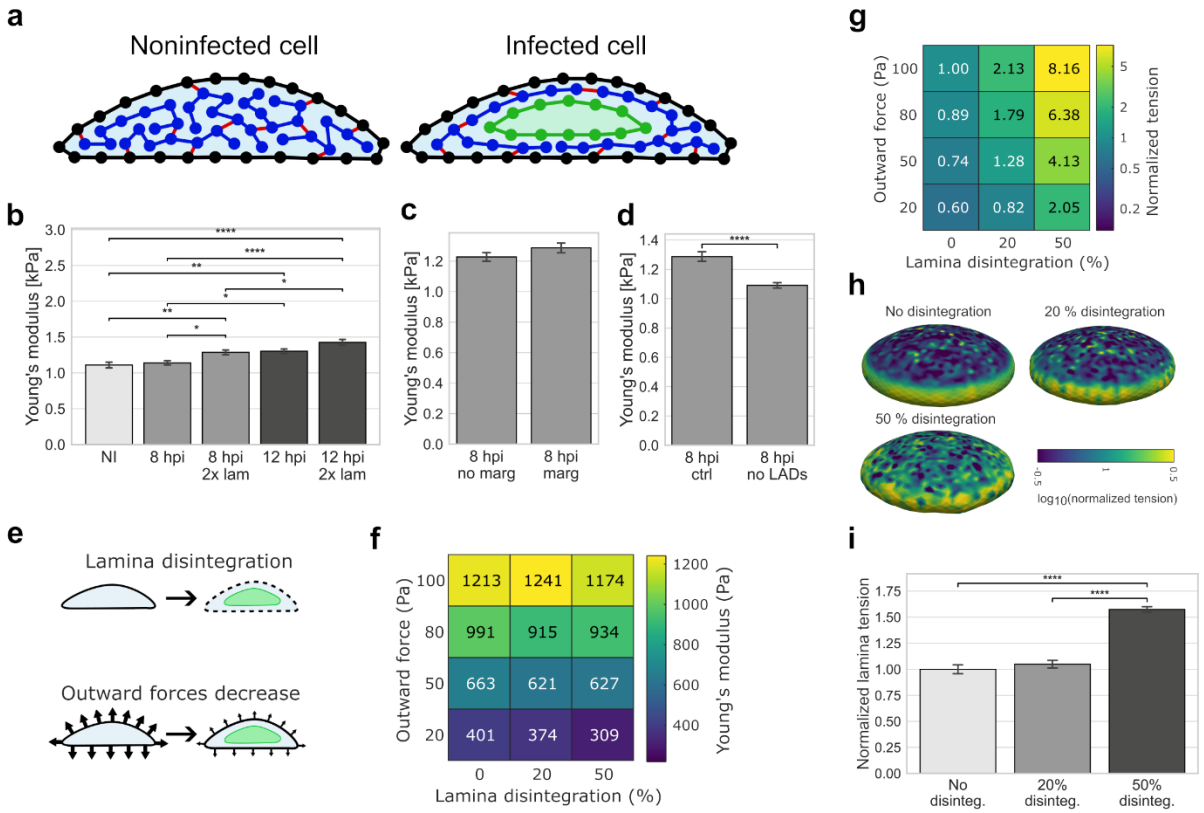

Figure 6. Changes in mechanical parameters alter the nuclear stiffness.
(a) The setup for the computational model shows noninfected and infected nuclei. The nuclear envelope (NE) (black line), chromatin polymers (blue), envelope-chromatin and chromatin-chromatin connections (red lines), and the viral replication compartment (VRC) (green line) are shown. (**b**) Simulated Young's moduli for the noninfected (NI) and infected cells (8 and 12 hpi), (**c**) for the infected nuclei (8 hpi) without and with chromatin marginalization close to the NE, and **(d)** for the infected nuclei with and without lamina-associated domains (LADs) (n=24). The lamina strength was doubled for (b) and (c) compared to NI. (**e**) Simulation of two changes in the nuclear mechanical parameters: lamina disintegration and decrease in the outward forces. **(f)** Simulated Young's moduli as a function of parameters in infected cell nuclei at 8 hpi with double the lamina strength compared to NI (n=8). Significances are shown in Supplementary Figure S3. **(g)** Normalized membrane tension as a function of lamina disintegration and a decrease in outward forces (n=8). Significances are shown in Supplementary Figure S3. (**h**) Representative examples of lamina forces with no lamina disintegration, and 20% and 50% disintegration. (**i**) The sum of normalized lamina forces on the top surface of the nuclei without or with 20% or 50% disintegration (normalized to the mean value with no disintegration) (n=8). Statistical significances were determined using Tukey's test (b,i) or Student's t-test (c,d). The significance values shown are denoted as **** ($p<0.0001$), *** ($p<0.001$), ** ($p<0.01$), * ($p<0.05$). Nonsignificant differences ($p \geq 0.05$) are not labeled.

DISCUSSION

The progression of HSV-1 infection and expansion of the viral replication complex led to remodeling of the nuclear structures and mechanical properties. Our experimental data, supported by the computational model, suggested qualitative and quantitative patterns of virus-induced structural reorganization, which led to softening of the nucleus.

The measured Young's moduli during the infection decreased until 8 hpi and then increased to some extent at 10 hpi. There are no previous studies of virus-induced changes in nuclear elasticity besides one study in isolated nuclei showing that the genome ejection into the nucleus increases nuclear stiffness[58]. Our data shows that this is at most a transitory phenomenon, since at 4 hpi the nuclear stiffness was smaller than in noninfected cells. There are many candidate mechanisms for the observed nuclear softening. These are, for example, changes in the nuclear structure caused by the massive VRC appearing at the center of the nucleus, changes in the nuclear lamina, a decrease in the osmotic pressure, or a decrease in the external pull by the cytoskeleton.

The progression of HSV-1 infection leads to the formation of an enlarged nuclear VRC. At late stages of infection, the VRC can occupy one-third of the nuclear volume[26]. The morphology of VRCs, their capability to fuse[59], and the enrichment of viral immediate early proteins into them[60] suggest that they are formed by liquid-liquid phase separation (LLPS)[61,62]. Our SXT results indicate that the VRC region is less dense than the euchromatin region in noninfected cells and the marginalized chromatin in infected cells. This shows that HSV-1 infection forms an expanded low-density nuclear center surrounded by chromatin. It is known that for many

materials density is proportional to their stiffness[63], so it is possible that the lower density of the VRC, compared to the chromatin, contributes to the nuclear softening during the infection.

Studies with lamin A/C-deficient yeast cells have shown that the chromatin tethering to the nuclear membrane increases the mechanical stiffness of the NE, and untethering of the chromatin leads to a softer nucleus[9]. It has remained unclear how the infection and enlarged VRC affect the intranuclear ion and osmotic concentration. Modeling has stated that nuclear osmotic pressure is proportional to its macromolecular concentration[64,65]. Thus, the reduced macromolecular concentration in the VRC region likely participates in regulating nuclear stiffness via osmotic pressure decrease.

One of the major regulators of nuclear stiffness is the nuclear lamina associated with peripheral heterochromatin, particularly lamins A and C[12,14,47,66–69]. Our studies show that nuclear lamins can directly contribute to regulating nuclear growth both in noninfected and infected cells. The overexpression of lamin A leads to an increased nuclear volume, whereas the expression of mutant lamin A, progerin, results in decreased nuclear volume. The nuclear enlargement of infected cells is also supported by the upregulation of the genes encoding for lamins A/C, B1, and B2 at early infection and the increased presence of these long-lived proteins[70] later in infection. The nuclear expansion might also explain why the marginalized chromatin does not become denser than the heterochromatin of the control cells.

Increased expression of lamin A has been linked to an increase in nuclear stiffness[71]. However, this effect might be counteracted by the virus-induced modification of the nuclear lamina. Herpesvirus infection results in local dispersion of the nuclear lamina by phosphorylation and redistribution of lamins A/C and B. Various viral proteins and kinases (UL13, UL34, ICP34.5,

and Us3) mediate these processes[37,72–75]. We showed how the mobility of the nuclear lamina decreases in infection, suggesting a possible increase in the tension or rigidity of the NE. However, it cannot be ruled out that infection-induced changes in the microtubules might also play a role in the nuclear envelope mobility[9]. Our simulations showed that the effect of lamina disintegration was not significant on simulated nuclear stiffness alone, but it became relevant when the outward forces were reduced. Finally, we showed that the nuclear membrane tension increases at late infection simultaneously with the expansion of the nuclear volume. This could be explained by earlier studies showing that nuclear swelling induces mechanical stretching forces that lead to elevated membrane tension[76]. In addition, our simulation showed that the disintegration of the lamina led to increased membrane tension, as more of the outward forces were subjected to the membrane rather than the lamina.

The nuclear elasticity is also regulated by the cytoskeletal tension mediated by the LINC complex linking the nucleo- and cytoskeleton[12,69,14]. The suppression of LINC protein SUN2 leads to changes in nuclear mechanical properties and causes nuclear softening[77]. A deficiency of both SUN1 and SUN2 proteins causes a decrease in nuclear size and an increase in nuclear elasticity[78]. SUN2 is a short-lived protein with a degradation half-life of 240 min[79]. Our data show that the progression of HSV-1 infection leads to a strong downregulation of SUN2. This most likely regulates the mechanical properties of the nucleus and decreases the nuclear stiffness as the infection proceeds. SUN2 depletion also leads to the modification of the NE double membrane and the perinuclear space. In HSV-1 infection, decreased expression of SUN2 supports the progression of infection and results in increased production of HSV-1 extracellular capsids, possibly by enhancing the NE modifications during the nuclear egress of capsids through it[80].

In our simulations, conducted to explain the experimental softening of the nucleus, the reduction of the outward forces caused the most significant reduction in the nuclear stiffness, suggesting that this could be the main mechanism for the experimentally observed change in stiffness during the infection. The outward forces described the combined effect of cytoskeletal forces on the NE, mediated by the LINC complex and SUN2, as well as the osmotic pressure. Also, the downregulation of the essential LINC protein SUN2 could partly explain the decreased stiffness. In addition, the low-density VRC leading to decreased osmotic pressure in the nuclear center could also affect the measured reduction of Young's modulus observed in the AFM measurements. However, we cannot rule out the possibility that the mechanical changes in the cell cytoskeleton, that were omitted from this study, would also affect the nuclear stiffness, especially since HSV-1 is known to rearrange actin cytoskeleton via cofilin-1[81]. The chromatin tethering close to the NE increasing the stiffness of the nucleus seems to counteract the nuclear softening; however, it seems insufficient to resist other forces that increase nuclear elasticity.

Our experimental data shows that the progression of infection affects intracellular mechanical forces that regulate nuclear stiffness. These changes include the emergence of low-density VRC, reorganization of chromatin, nuclear lamina, and interactions between cytoplasm and nucleus. Altogether, the profound, virus-induced deformation of the nuclear organization and mechanics softens the nucleus. Our simulations show that the measured changes in the nuclear lamina and volume have quite a minor effect on Young's modulus compared to the nucleocytoplasmic forces, namely cytoskeletal-nuclear connections and osmotic pressure.

MATERIALS AND METHODS

Cells and viruses

Mouse embryonic fibroblast cells (MEF, ATCC® CRL-2991™) and African green monkey kidney cells (Vero, ATCC® CCL-81™) were grown in Dulbecco's modified Eagle medium (DMEM) supplemented with 10% fetal bovine serum, L-glutamine and penicillin-streptomycin (Gibco-Invitrogen, Carlsbad, CA*)* at 37 °C in the presence of 5% CO_2. HA-tagged progerin, a truncated version of lamin A[82], was expressed in the Vero cells using adenovirus[83]. Lamin A adenovirus was used to overexpress wild-type lamin A in Veros. Lamin A adenovirus (based on RefSeq BC014507) was purchased from Vector Biolabs and used as previously described[83]. The cells were infected 4, 8, or 12 hours before imaging and measurements with wild-type 17+ strain, EYFP-ICP4 (vEYFP-ICP4[84]), or VP26-mCherry virus (HSV1(17^+)Lox-CheVP26)[85–87] using a multiplicity of infection of 5.

Atomic force microscopy (AFM)

Force spectroscopy AFM experiments were performed on an AFM NanoWizard 4xp instrument (JPK BioAFM, Bruker Nano GmbH, Berlin, Germany) mounted on an inverted microscope (Nikon Ti-U, Nikon Instruments Europe B.V, Amsterdam, the Netherlands) equipped with a standard monochrome CCD camera (ProgRes MFCool, Jenoptik, Jena, Germany). Fluorescence imaging was performed by wide-field illumination (Intensilight Hg lamp, Nikon) with a 100X objective (Nikon CFI Apo VC, 1.4 NA, oil immersion) and the appropriate filter cube for EYFP fluorescence. A software module (DirectOverlay, JPK Bio-AFM, Bruker Nano GmbH, Berlin, Germany) calibrated the tip position with the optical image. Nanomechanical measurements were performed in spectroscopy mode using 6.62 μm (CP-PNPL-SiO-C from SQube, mean cantilever spring constant kcant = 0.06 N/m). Before each set of acquisitions, the sensitivity and spring constant of the cantilever was calibrated (thermal

noise method). The measurements were performed in the buffered culture medium at 37°C with an injection of 5% CO2, with a relative setpoint of 2 nN, a Z-length of 12µm, and a constant extend velocity of 1 µm/s. The center of the nucleus of a cell was visualized by fluorescence and measured ten times in a row. Raw data have been cleaned manually by removing any aberrant contact point, and each force curve has been fit were cleaned manually by removing any aberrant contact point, and each force curve was fitted with a Hertz model to calculate the Young's modulus using JPK data Processing software (7.0.181). The average measures were plotted by cell (one point is one cell) after filtering out outliers (zscore>3).

Cryo-soft X-ray tomography (SXT) of suspended cells in capillaries

Vero cells were seeded into culture flasks (Corning, Corning, NY) and infected with HSV-1 vEYFP-ICP4 at an MOI of 5 for 8 hours at 37°C. Noninfected and infected cells were detached with trypsin-EDTA, pelleted by centrifugation (300xg), and washed with PBS. Cells were then fixed with glutaraldehyde (0.5%) and paraformaldehyde for 10 minutes at RT and 35 minutes at 4°C (4%, cat. No. 15713-S; Electron Microscopy Sciences, Hatfield, PA), washed once with PBS, pelleted by centrifugation (300x*g*), re-suspended in the PBS buffer, filtered, loaded into thin-walled cylindrical borosilicate glass capillaries (Hilgenberg GmbH, Hilgenberg, GER, Cat.No. 4023088), and then vitrified by quickly plunging them into liquid-nitrogen-cooled (~90 K) liquid propane. SXT tomographic data were collected by full-rotation imaging with a soft X-ray microscope (XM-2) in the National Center for X-ray Tomography at the Advanced Light Source (http://www.als.lbl.gov) of Lawrence Berkeley National Laboratory (Berkeley, CA). Cells were kept in a stream of liquid-nitrogen-cooled helium gas to avoid radiation damage during data collection. For each data set, 180° rotation tomographs (1 projection image per 2° angle) were collected[88,89]. Projection images were aligned by tracking fiducial markers on adjacent images and reconstructed using automatic reconstruction software[90]. The

segmentation of the high- and low-density chromatin was realized using the histogram separation in two classes by DragonFly.

Focused Ion Beam Scanning Electron Microscopy **(FIB-SEM)**

The volume imaging data set of MEFs having enhanced contrast on chromatin was generated by FIB-SEM. MEFs, noninfected or HSV-1 infected at MOI of 5 for 8 h, were processed for imaging as described earlier (Leclerc et al. 2024). The Chrom EM method enhanced the contrast of DNA, including staining with DRAQ5 (Ou et al. 2017). The deposition of the osmiophilic polymer of diaminobenzidine, specifically on the DNA, was carried out using fluorescent emission of DRAQ5. For this, the cells were placed on a cooled stage of Leica DM IL LED microscope and exposed to 620 $\pm$ 30 nm light in the presence of diaminobenzidine, inducing its local polymerization over DRAQ5 bound DNA. The cells were treated with osmium tetraoxide followed by dehydration with a graded series of ethanol and embedding in resin. One set of cells was thin-sectioned and then poststained with 2 % uranyl acetate and lead citrate. Another set of cells was coated with platinum. The sections were imaged using a Jeol JEM – 1400HC transmission electron microscope with an Olympus SIS Quemesa bottom-mounted charge-coupled device camera (80 kV). The datasets were acquired in a Zeiss Crossbeam 500 using backscattered and secondary electron signals. The area of interest was exposed by a milling beam (0.7 nA at the accelerating voltage of 30 kV) and imaged by scanning electron beam (0.31 or 0.50 nA, 1.5 or 1.6 keV). The milling and scanning process on the cross-section of the cell created an image volume having a voxel size of 2.5 x 2.5 x 5 nm^3. The datasets were collected and aligned using Zeiss Atlas 5 software with a 3D tomography module. Microscopy Image Browser[91] processed and segmented the capsids, chromatin, and nuclear envelope. The chromatin segmentation was done semi-automatically using MIB (https://mib.helsinki.fi/) and then cleaned by iterative intensity-based erosion. The

local thickness of the chromatin was measured using ImageJ (https://imagej.net/imagej-wiki-static/Local_Thickness) in Python, the local maxima were identified, and the local thickness value was extracted. The distance of these local maxima to the nuclear envelope was then calculated using the Euclidean distance transform.

Confocal imaging and analysis

Wild-type Vero cells, Vero cells expressing HA-tagged progerin, or overexpressing wild-type lamin A were grown on glass coverslips for microscopy to analyze the nuclear volume. The cells were infected with HSV-1 EYFP-ICP4 and fixed at 4, 8, and 12 hpi with 4% PFA, and DNA was labeled with DAPI. Viral EYFP-ICP4 was boosted with anti-GFP antibody. Cells were embedded into VECTASHIELD® PLUS Antifade Mounting Medium (H-1900) (Vector Laboratories). The cells were imaged using a Leica SP8 confocal microscope with UPLSAPO 63x oil immersion objective (NA 1.35). DAPI (Invitrogen) was excited with a 405 nm diode laser, and a 410-439 nm band pass filter was used to detect the fluorescence. EYFP was excited with a 488 nm laser, and the fluorescence was collected with a 519-540 nm bandpass filter. Lamin A/C was excited with a 653 nm laser and fluorescence was collected with 661-839 nm filter. Stacks of 1024 x 1024 pixels were collected with a 120 nm/pixel pixel size in the x- and y- directions and 400 nm in the z-direction. The nuclei were segmented using the minimum cross entropy threshold algorithm[92] for the DAPI channel.

For analyses of the nuclear intensity of lamins, Vero cells infected with HSV-1 EYFP-ICP4 and fixed at 8 and 12 hpi were labeled with antibodies against lamin A/C (mouse monoclonal antibody MAb; ab8984, Abcam, Cambridge, UK) and Lamin B (rabbit polyclonal antibody, rAb; ab16048, Abcam). The primary antibodies were followed by goat anti-rabbit or anti-mouse Alexa 488- and 647-conjugated secondary antibodies (Thermo Fisher Scientific,

Waltham, MA, USA). DNA was labeled with Hoechst 1:10000 in PBS for 10 min. Cells were embedded into VECTASHIELD® PLUS Antifade Mounting Medium (H-1900) (Vector Laboratories). The immunolabeled cells were imaged using a Leica TCS SP8 FALCON laser scanning confocal microscope (Leica Microsystems, Mannheim, Germany). Alexa 546 and Alexa 647 were excited with 557 nm and 653 nm wavelengths of pulsed white light laser (80 MHz), respectively. The emission detection range was 568-648 nm for Alexa 546 and 663-776 nm for Alexa 647. DAPI was excited with a 405 nm diode laser, and emission between 415-495 nm was detected. Laser powers for all channels were fixed. Stacks of 1024 x 1024 pixels were collected with 120 nm/pixel in the x- and y- directions and 240 nm in the z-direction. The nuclei were segmented using minimum cross entropy threshold algorithm[92] for the DAPI channel. The total nuclear intensity was calculated for the pixels belonging to the segmented nucleus, and the intensity near the NE was calculated by using only pixels having Euclidean distance of 1 μm or less from the NE.

The distribution and mobility of lamins were analyzed in living noninfected and HSV-1 mCherry infected (8, 12 hpi) Vero cells transfected with expressing lamin A/C-Chromobody-GFP2 (Proteintech, Manchester, UK) using Leica HC PL APO CS2 1.2NA 63X water immersion objective. During the imaging with Leica SP8 Falcon, the lamin A/C-Chromobody-GFP2 was excited with 488 nm wavelength of pulsed white light laser (80 MHz). The emission detection range was 495-560 nm for GFP2. DAPI was excited with a 405 nm diode laser, and emission between 412-475 nm was detected. The image stack size was 296 x 296 pixels with a 100 nm/pixel size in the x- and y-directions. The lamina was analyzed by first removing translational and rotational motion of it. The lamina was skeletonized at each time point, and then the maximum intensity projection of the skeletons was taken. The area of the maximum intensity projection was calculated and divided by the length of it. The curvature was defined

by discretizing the nuclear lamina using 16-pixel (1.6 µm) long line segments and calculating the angles between consecutive segments.

Nuclear membrane tension was measured and analyzed by fluorescent lifetime imaging (FLIM) using fluorescent membrane tension probe ER Flipper-TR® (Spirochrome) in noninfected and HSV-1 17+ wt infected live Vero cells at 8, and 12 hpi. Measurements were performed with Leica SP8 Falcon with Leica HyD SMD detectors and Leica HC PL APO CS2 1.2NA 63X water immersion objective. The ER Flipper probe was used in 1µM concentration and the cells were also labelled using Hoechst 33342 in 1µM concentration. One plane at the center of the nucleus, where the nuclear edges were clearly identified, was first acquired with 405 nm excitation and 415-465 nm emission to visualize cell DNA with Hoechst. Immediately after, the ER Flipper was acquired using 477 nm excitation and 550-650 nm emission and line accumulation of 16. Scanning speed was 200Hz, repetition rate 80MHz, image size 328x328 pixels and 81x81nm/pixel for both Hoechst and ER Flipper imaging. For tension analysis, pixel binning of 3 was used resulting in approximately 500-1500 photons per pixel. After binning, a pixel-wise two-component fitting was performed and the longer component describing the membrane tension was extracted. Using the Hoechst data, a 486 nm wide ring just outside the cellular DNA was used as a mask to obtain the nuclear membrane area from the tension data (Fig. 4A). A mean of the longer ER Flipper lifetime along the nuclear envelope was calculated for each cell.

To measure the contact area of the cells during the infection, ICP4-EYFP-infected cells were labeled using mouse Anti-beta Actin antibody [mAbcam 8226], abcam, (ab8226). The contact area of the cells during the infection was analyzed by taking the sum projection in the z-

direction of the actin channel, thresholding the sum projection using minimum cross entropy algorithm[92], and calculating the area of the segmented region.

Global Run-On and sequencing (GRO-seq)

Noninfected and infected Vero cells (at 4, 8 hpi) were suspended in a swelling buffer (10 mM Tris-HCl, 2 mM MgCl2, 3 mM CaCl2, 1 U/ml SUPERase-In and 1 U/ml RNAsin plus (RNAse inhibitor, Thermofisher, Carlsbad, CA, USA; RNAse inhibitor, Promega, Madison, Wisconsin, USA) and allowed to swell for 5 minutes. Following this, they were centrifuged at 400 × g for 10 minutes, then resuspended in 500 µl of the same buffer, now supplemented with 10% glycerol and RNAse inhibitors. During gentle vortexing, an additional 500 µl of the glycerol-supplemented buffer with 1% Igepal was gradually added to the cell suspension.

The nuclei underwent two washes using the swelling buffer enhanced with 0.5% Igepal and 10% glycerol. This was followed by a single wash with a freezing buffer comprising 50 mM Tris-HCl (pH 8.3), 40% glycerol, 5 mM MgCl2, and 0.1 mM EDTA. After counting, the nuclei were centrifuged at 900 × g for 6 minutes, resuspended to yield a concentration of 5 million nuclei/100 µl in freezing buffer, snap-frozen, and stored at -80°C until further use.

The nuclear run-on reaction buffer (NRO-RB) containing 496 mM KCl, 16.5 mM Tris-HCl, 8.25 mM MgCl2, and 1.65% Sarkosyl (Sigma-Aldrich, Steinheim, Germany) was pre-warmed to 30°C. To each milliliter of NRO-RB, 1.5 mM DTT, 750 µM each of ATP and GTP, 4.5 µM CTP, 750 µM Br-UTP (Santa Cruz Biotechnology, Dallas, Texas, USA), and 33 µl of SUPERase Inhibitor (Thermo Fischer Scientific) were added. This supplemented NRO-RB (50 µl) was mixed with 100 µl of the nuclear samples, and the mixture was incubated at 30°C for 5 minutes.

The preparation of GRO-Seq libraries followed the protocol from Kaikkonen et al. (2014). In summary, the run-on products underwent DNAse I treatment (TURBO DNA-free Kit, Thermo

Fischer Scientific), base hydrolysis (RNA fragmentation reagent, Thermo Fischer Scientific), end-repair, and immuno-purification using Br-UTP beads (Santa Cruz Biotechnology). After that, a poly-A tailing reaction was performed (PolyA polymerase, New England Biolabs), followed by steps of circularization and re-linearization. The cDNA templates were PCR amplified (Illumina barcoding) for 11-14 cycles and size-selected to range between 180-300 bp. The final libraries were quantified using a Qubit fluorometer (Thermo Fischer Scientific) and readied for 50 bp single-end sequencing on an Illumina Hi-Seq2000 platform (GeneCore, EMBL Heidelberg, Germany). Post-sequencing, GRO-Seq reads were processed using HOMER software2 to eliminate A-stretches arising from the library preparation and to discard sequences shorter than 25 bp. The quality of the raw sequencing reads was first assessed using the FastQC tool (http://www.bioinformatics.babraham.ac.uk/projects/fastqc/). Bases failing to meet quality standards, specifically those reads where less than 97% of bases had a minimum phred quality score of 10, were trimmed utilizing the FastX toolkit (http://hannonlab.cshl.edu/fastx_toolkit/). For samples sequenced across multiple lanes, data were combined post-quality control. GRO-seq reads were aligned to the ChlSab1.1 genome using the bowtie-0.12.7 software (Langmead et al. 2009). while allowing up to two mismatches and up to three locations per read, the best alignment was reported. Differentially expressed genes were detected using ChlSab1.1.95.gtf coordinates, and the RNA.pl workflow of HOMER 4.3 and edgeR v3.2.2 was analyzed. Genes were considered differentially expressed using the following cutoffs: log2 fold change 0.585, RPKM 0.5 in at least one sample, and adjusted p-value of 0.05. GRO-seq reads were mapped to the human protein atlas (https://www.proteinatlas.org/) to select lamin a/c and nuclear lamina-related proteins. The interaction of these proteins was further mapped using the String database (https://string-db.org/) by selecting experimentally shown interaction using a threshold of 500. The non-interacting proteins have been identified in the same String database with the condition that

they interact with at least 1 detected protein. The resulting graph has been generated in Python using the module network and manually adjusted.

Computational modeling

The developed computational model described the nucleus as a separate NE, which was considered to include the lamina, and chromatin components in three dimensions. The main model assumptions were: (1) the mechanical properties of the nucleus are dictated by the nuclear envelope, chromatin, and outward forces, including actin cytoskeleton prestress and osmotic pressure difference; (2) no changes in the mechanical properties occur during the short AFM measurement; and (3) the VRC has low density and has no effect on the AFM measurement. The envelope was triangulated into a viscoelastic shell, and self-avoiding polymer chains described the chromatin. Furthermore, additional interactions were defined to describe various connections, such as the LADs between the chromatin and the lamina and those between different parts of the chromatin. The Herpes VRC was described as a single coherent entity within the nucleus. It was represented similarly to the nuclear envelope as a triangulated shape that repulses the chromatin while it grows.

The model is simulated by calculating a force affecting each vertex originating from various, usually Hookean, interactions and moving them using the dampened equation of motion:

$$\gamma \vec{v}_i + \sum_j c_{ij} \left(\vec{v}_i - \vec{v}_j \right) = \vec{F}_i + \eta,$$

where γ is the system viscosity, $\vec{v}_i$ the velocity of vertex i, c_{ij} the friction between vertices i and j, $\vec{F}_i$ the total force affecting vertex i, and η the random thermal motion. The equation is solved using the conjugate gradient and the vertex movements using the forward Euler method.

To simulate the AFM experiments, a cantilever with properties mirroring those of the one used in the experiments was used to push down on the nucleus, and the resulting force and indentation depth data was used to calculate the Young's modulus using the Hertz model. The computational model was implemented using Julia programming language (v1.10.2), and the model and the parameters are described in more detail in the Supplementary Text 1. The code is available in Github (https://github.com/atervn/nuclear_mech) and Zenodo (https://zenodo.org/records/14512358). The data fitting for the Hertz model was done using Matlab (The MathWorks Inc, R2021a, Natick, Massachusetts) and 3D visualization using ParaView[93].

Data availability

The authors declare that the GRO-Seq data were deposited into the Gene Expression Omnibus database under accession number GSE243613 and are available at https://www.ncbi.nlm.nih.gov/geo/query/acc.cgi?acc=GSE243613. All other relevant data are in the manuscript and its supporting information files.

Contributions

Conceptualization: Aapo Tervonen, Teemu Ihalainen, Vesa Aho, Maija Vihinen-Ranta

Data curation: Aapo Tervonen, Visa Ruokolainen, Simon Leclerc, Henri Niskanen, Minna Kaikkonen, Vesa Aho

Formal analysis: Aapo Tervonen, Visa Ruokolainen, Simon Leclerc, Henri Niskanen, Vesa Aho

Funding Acquisition: Daniel Conway, Teemu Ihalainen, Maija Vihinen-Ranta

Investigation: Aapo Tervonen, Visa Ruokolainen, Simon Leclerc, Katie Tieu, Jian-Hua Chen, Sébastien Lyonnais, Henri Niskanen, Salla Mattola, Vesa Aho

Methodology: Jian-Hua Chen, Sébastien Lyonnais, Daniel Conway

Resources: Delphine Muriaux, Carolyn A. Larabell, Minna Kaikkonen

Software: Simon Leclerc, Vesa Aho

Project Administration: Maija Vihinen-Ranta

Visualization: Visa Ruokolainen, Simon Leclerc, Katie Tieu, Jian-Hua Chen, Sébastien Lyonnais, Alka Gupta, Salla Mattola

Writing – Original Draft Preparation: Aapo Tervonen, Maija Vihinen-Ranta, Vesa Aho

Writing – Review & Editing: Aapo Tervonen, Visa Ruokolainen. Daniel Conway, Teemu Ihalainen, Vesa Aho, Maija Vihinen-Ranta

Ethical statement

The experiments were done using commercially available cell lines without ethical challenges.

Competing interests

The authors have declared that no competing interests exist.

Funding information

This work was financed by the Jane and Aatos Erkko Foundation (MVR); Academy of Finland under award number 330896 (MVR); European Union's Horizon 2020 research and innovation program under grant agreement No 101017116, project CoCID (Compact Cell-Imaging Device, MVR); National Institute of Health award R35 GM119617 (DEC).

The funders had no role in the study design, data collection and analysis, the decision to publish, or the preparation of the manuscript.

Acknowledgment

We thank the staff of the National Center for X-ray Tomography (NCXT) and Advanced Light Source (Lawrence Berkeley National Laboratory, Berkeley, CA) for providing cryo-SXT experiments. We thank Helena Vihinen from Electron microscopy Unit (University of Helsinki, Institute of Biotechnology, Helsinki Institute of Life Science, Helsinki, Finland) for FIB-SEM sample preparation and imaging. We thank Elina Mäntylä for GRO-Seq sample preparation.

REFERENCES

1. Carley, E. *et al.* The LINC complex transmits integrin-dependent tension to the nuclear lamina and represses epidermal differentiation. *eLife* **10**, e58541.
2. Vining, K. H. & Mooney, D. J. Mechanical forces direct stem cell behaviour in development and regeneration. *Nat Rev Mol Cell Biol* **18**, 728–742 (2017).
3. Uhler, C. & Shivashankar, G. V. Regulation of genome organization and gene expression by nuclear mechanotransduction. *Nat Rev Mol Cell Biol* **18**, 717–727 (2017).
4. Versaevel, M., Grevesse, T. & Gabriele, S. Spatial coordination between cell and nuclear shape within micropatterned endothelial cells. *Nat Commun* **3**, 671 (2012).
5. McCreery, K. P. *et al.* Nuclear Stiffness Decreases with Disruption of the Extracellular Matrix in Living Tissues. *Small* **17**, e2006699 (2021).
6. Lammerding, J. Mechanics of the nucleus. *Compr Physiol* **1**, 783–807 (2011).
7. Moore, H. M. & Vartiainen, M. K. F-actin organizes the nucleus. *Nat Cell Biol* **19**, 1386–1388 (2017).
8. Pajerowski, J. D., Dahl, K. N., Zhong, F. L., Sammak, P. J. & Discher, D. E. Physical plasticity of the nucleus in stem cell differentiation. *Proc Natl Acad Sci U S A* **104**, 15619–15624 (2007).
9. Schreiner, S. M., Koo, P. K., Zhao, Y., Mochrie, S. G. J. & King, M. C. The tethering of chromatin to the nuclear envelope supports nuclear mechanics. *Nat Commun* **6**, 7159 (2015).
10. Turgay, Y. *et al.* The molecular architecture of lamins in somatic cells. *Nature* **543**, 261–264 (2017).
11. Vahabikashi, A., Adam, S. A., Medalia, O. & Goldman, R. D. Nuclear lamins: Structure and function in mechanobiology. *APL Bioeng* **6**, 011503 (2022).

12. Lammerding, J. *et al.* Lamin A/C deficiency causes defective nuclear mechanics and mechanotransduction. *J Clin Invest* **113**, 370–378 (2004).

13. Gruenbaum, Y. & Foisner, R. Lamins: nuclear intermediate filament proteins with fundamental functions in nuclear mechanics and genome regulation. *Annu Rev Biochem* **84**, 131–164 (2015).

14. Dahl, K. N., Kahn, S. M., Wilson, K. L. & Discher, D. E. The nuclear envelope lamina network has elasticity and a compressibility limit suggestive of a molecular shock absorber. *J Cell Sci* **117**, 4779–4786 (2004).

15. Stephens, A. D., Banigan, E. J., Adam, S. A., Goldman, R. D. & Marko, J. F. Chromatin and lamin A determine two different mechanical response regimes of the cell nucleus. *Mol Biol Cell* **28**, 1984–1996 (2017).

16. Stephens, A. D. *et al.* Chromatin histone modifications and rigidity affect nuclear morphology independent of lamins. *Mol Biol Cell* **29**, 220–233 (2018).

17. Stephens, A. D. *et al.* Physicochemical mechanotransduction alters nuclear shape and mechanics via heterochromatin formation. *Mol Biol Cell* **30**, 2320–2330 (2019).

18. Mazumder, A., Roopa, T., Basu, A., Mahadevan, L. & Shivashankar, G. V. Dynamics of chromatin decondensation reveals the structural integrity of a mechanically prestressed nucleus. *Biophys J* **95**, 3028–3035 (2008).

19. Strom, A. R. *et al.* HP1α is a chromatin crosslinker that controls nuclear and mitotic chromosome mechanics. *Elife* **10**, e63972 (2021).

20. Dos Santos, Á. *et al.* DNA damage alters nuclear mechanics through chromatin reorganization. *Nucleic Acids Res* **49**, 340–353 (2021).

21. Deviri, D. & Safran, S. A. Balance of osmotic pressures determines the nuclear-to-cytoplasmic volume ratio of the cell. *Proc Natl Acad Sci U S A* **119**, e2118301119 (2022).

22. Kobiler, O. & Weitzman, M. D. Herpes simplex virus replication compartments: From naked release to recombining together. *PLoS Pathog* **15**, e1007714 (2019).

23. Church, G. A., Dasgupta, A. & Wilson, D. W. Herpes simplex virus DNA packaging without measurable DNA synthesis. *J Virol* **72**, 2745–2751 (1998).

24. Heming, J. D., Conway, J. F. & Homa, F. L. Herpesvirus Capsid Assembly and DNA Packaging. *Adv Anat Embryol Cell Biol* **223**, 119–142 (2017).

25. Monier, K., Armas, J. C., Etteldorf, S., Ghazal, P. & Sullivan, K. F. Annexation of the interchromosomal space during viral infection. *Nat Cell Biol* **2**, 661–665 (2000).

26. Aho, V. *et al.* Quantitative Microscopy Reveals Stepwise Alteration of Chromatin Structure during Herpesvirus Infection. *Viruses* **11**, 935 (2019).

27. McSwiggen, D. T. *et al.* Evidence for DNA-mediated nuclear compartmentalization distinct from phase separation. *Elife* **8**, e47098 (2019).

28. Seyffert, M. *et al.* The HSV-1 Transcription Factor ICP4 Confers Liquid-Like Properties to Viral Replication Compartments. *Int J Mol Sci* **22**, 4447 (2021).

29. Caragliano, E. *et al.* Human cytomegalovirus forms phase-separated compartments at viral genomes to facilitate viral replication. *Cell Rep* **38**, 110469 (2022).

30. Aho, V. *et al.* Chromatin organization regulates viral egress dynamics. *Sci Rep* **7**, 3692 (2017).

31. Aho, V. *et al.* Infection-induced chromatin modifications facilitate translocation of herpes simplex virus capsids to the inner nuclear membrane. *PLoS Pathog* **17**, e1010132 (2021).

32. Bosse, J. B. *et al.* Remodeling nuclear architecture allows efficient transport of herpesvirus capsids by diffusion. *Proc Natl Acad Sci U S A* **112**, E5725-5733 (2015).

33. Lewis, H. C. *et al.* HSV-1 exploits host heterochromatin for nuclear egress. *J Cell Biol* **222**, e202304106 (2023).

34. Mettenleiter, T. C., Müller, F., Granzow, H. & Klupp, B. G. The way out: what we know and do not know about herpesvirus nuclear egress. *Cell Microbiol* **15**, 170–178 (2013).

35. Simpson-Holley, M., Baines, J., Roller, R. & Knipe, D. M. Herpes simplex virus 1 U(L)31 and U(L)34 gene products promote the late maturation of viral replication compartments to the nuclear periphery. *J Virol* **78**, 5591–5600 (2004).

36. Bigalke, J. M., Heuser, T., Nicastro, D. & Heldwein, E. E. Membrane deformation and scission by the HSV-1 nuclear egress complex. *Nat Commun* **5**, 4131 (2014).

37. Bjerke, S. L. & Roller, R. J. Roles for herpes simplex virus type 1 UL34 and US3 proteins in disrupting the nuclear lamina during herpes simplex virus type 1 egress. *Virology* **347**, 261–276 (2006).

38. Bahnamiri, M. M. & Roller, R. J. Mechanism of Nuclear Lamina Disruption and the Role of pUS3 in HSV-1 Nuclear Egress. *J Virol* **95**, e02432-20, JVI.02432-20 (2021).

39. Schäpe, J., Prausse, S., Radmacher, M. & Stick, R. Influence of lamin A on the mechanical properties of amphibian oocyte nuclei measured by atomic force microscopy. *Biophys J* **96**, 4319–4325 (2009).

40. Hobson, C. M. *et al.* Correlating nuclear morphology and external force with combined atomic force microscopy and light sheet imaging separates roles of chromatin and lamin A/C in nuclear mechanics. *Mol Biol Cell* **31**, 1788–1801 (2020).

41. Hobson, C. M., Falvo, M. R. & Superfine, R. A survey of physical methods for studying nuclear mechanics and mechanobiology. *APL Bioeng* **5**, 041508 (2021).

42. Kobiler, O., Brodersen, P., Taylor, M. P., Ludmir, E. B. & Enquist, L. W. Herpesvirus replication compartments originate with single incoming viral genomes. *mBio* **2**, e00278-11 (2011).

43. Chang, L. *et al.* Herpesviral replication compartments move and coalesce at nuclear speckles to enhance export of viral late mRNA. *Proc Natl Acad Sci U S A* **108**, E136-144 (2011).

44. Ou, H. D. *et al.* ChromEMT: Visualizing 3D chromatin structure and compaction in interphase and mitotic cells. *Science* **357**, eaag0025 (2017).

45. Jacob, R. J., Morse, L. S. & Roizman, B. Anatomy of herpes simplex virus DNA. XII. Accumulation of head-to-tail concatemers in nuclei of infected cells and their role in the generation of the four isomeric arrangements of viral DNA. *J Virol* **29**, 448–457 (1979).

46. De Sandre-Giovannoli, A. *et al.* Lamin a truncation in Hutchinson-Gilford progeria. *Science* **300**, 2055 (2003).

47. Lammerding, J. *et al.* Lamins A and C but not lamin B1 regulate nuclear mechanics. *J Biol Chem* **281**, 25768–25780 (2006).

48. Wang, Y. *et al.* GPCR-induced calcium transients trigger nuclear actin assembly for chromatin dynamics. *Nat Commun* **10**, 5271 (2019).

49. Goujon, A. *et al.* Mechanosensitive Fluorescent Probes to Image Membrane Tension in Mitochondria, Endoplasmic Reticulum, and Lysosomes. *J Am Chem Soc* **141**, 3380–3384 (2019).

50. Crisp, M. *et al.* Coupling of the nucleus and cytoplasm: role of the LINC complex. *J Cell Biol* **172**, 41–53 (2006).

51. Babatz, T. D. *et al.* Site specificity determinants for prelamin A cleavage by the zinc metalloprotease ZMPSTE24. *J Biol Chem* **296**, 100165 (2021).

52. Fu, B., Wang, L., Li, S. & Dorf, M. E. ZMPSTE24 defends against influenza and other pathogenic viruses. *J Exp Med* **214**, 919–929 (2017).

53. Stott-Marshall, R. J. & Foster, T. L. Inhibition of Arenavirus Entry and Replication by the Cell-Intrinsic Restriction Factor ZMPSTE24 Is Enhanced by IFITM Antiviral Activity. *Front Microbiol* **13**, 840885 (2022).

54. Serrano, J. B., da Cruz E Silva, O. A. B. & Rebelo, S. Lamina Associated Polypeptide 1 (LAP1) Interactome and Its Functional Features. *Membranes (Basel)* **6**, 8 (2016).

55. Luithle, N. *et al.* Torsin ATPases influence chromatin interaction of the Torsin regulator LAP1. *Elife* **9**, e63614 (2020).

56. Mackels, L., Liu, X., Bonne, G. & Servais, L. TOR1AIP1-Associated Nuclear Envelopathies. *Int J Mol Sci* **24**, 6911 (2023).

57. Wang, N., Tytell, J. D. & Ingber, D. E. Mechanotransduction at a distance: mechanically coupling the extracellular matrix with the nucleus. *Nat Rev Mol Cell Biol* **10**, 75–82 (2009).

58. Evilevitch, A. & Hohlbauch, S. V. Intranuclear HSV-1 DNA ejection induces major mechanical transformations suggesting mechanoprotection of nucleus integrity. *Proc Natl Acad Sci U S A* **119**, e2114121119 (2022).

59. Chang, L. *et al.* Herpesviral replication compartments move and coalesce at nuclear speckles to enhance export of viral late mRNA. *Proc Natl Acad Sci U S A* **108**, E136-144 (2011).

60. McSwiggen, D. T. *et al.* Evidence for DNA-mediated nuclear compartmentalization distinct from phase separation. *Elife* **8**, e47098 (2019).

61. Hyman, A. A., Weber, C. A. & Jülicher, F. Liquid-liquid phase separation in biology. *Annu Rev Cell Dev Biol* **30**, 39–58 (2014).

62. Caragliano, E. *et al.* Human cytomegalovirus forms phase-separated compartments at viral genomes to facilitate viral replication. *Cell Rep* **38**, 110469 (2022).

63. Ashby, M. F. & Bréchet, Y. J. M. Designing hybrid materials. *Acta Materialia* **51**, 5801–5821 (2003).

64. Finan, J. D., Chalut, K. J., Wax, A. & Guilak, F. Nonlinear osmotic properties of the cell nucleus. *Ann Biomed Eng* **37**, 477–491 (2009).

65. Zheng, S., Li, Y., Shao, Y., Li, L. & Song, F. Osmotic Pressure and Its Biological Implications. *Int J Mol Sci* **25**, 3310 (2024).

66. Neelam, S. *et al.* Direct force probe reveals the mechanics of nuclear homeostasis in the mammalian cell. *Proc Natl Acad Sci U S A* **112**, 5720–5725 (2015).

67. Davidson, P. M. & Lammerding, J. Broken nuclei--lamins, nuclear mechanics, and disease. *Trends Cell Biol* **24**, 247–256 (2014).

68. Broers, J. L. V. *et al.* Decreased mechanical stiffness in LMNA-/- cells is caused by defective nucleo-cytoskeletal integrity: implications for the development of laminopathies. *Hum Mol Genet* **13**, 2567–2580 (2004).

69. Gruenbaum, Y. & Foisner, R. Lamins: nuclear intermediate filament proteins with fundamental functions in nuclear mechanics and genome regulation. *Annu Rev Biochem* **84**, 131–164 (2015).

70. Buchwalter, A. Intermediate, but not average: The unusual lives of the nuclear lamin proteins. *Curr Opin Cell Biol* **84**, 102220 (2023).

71. Swift, J. *et al.* Nuclear lamin-A scales with tissue stiffness and enhances matrix-directed differentiation. *Science* **341**, 1240104 (2013).

72. Reynolds, A. E., Liang, L. & Baines, J. D. Conformational changes in the nuclear lamina induced by herpes simplex virus type 1 require genes U(L)31 and U(L)34. *J Virol* **78**, 5564–5575 (2004).

73. Mou, F., Forest, T. & Baines, J. D. US3 of herpes simplex virus type 1 encodes a promiscuous protein kinase that phosphorylates and alters localization of lamin A/C in infected cells. *J Virol* **81**, 6459–6470 (2007).

74. Takeshima, K., Maruzuru, Y., Koyanagi, N., Kato, A. & Kawaguchi, Y. Redundant and Specific Roles of A-Type Lamins and Lamin B Receptor in Herpes Simplex Virus 1 Infection. *J Virol* **96**, e0142922 (2022).

75. Leach, N. R. & Roller, R. J. Significance of host cell kinases in herpes simplex virus type 1 egress and lamin-associated protein disassembly from the nuclear lamina. *Virology* **406**, 127–137 (2010).

76. Enyedi, B., Jelcic, M. & Niethammer, P. The Cell Nucleus Serves as a Mechanotransducer of Tissue Damage-Induced Inflammation. *Cell* **165**, 1160–1170 (2016).

77. Yue, X. *et al.* Nuclear softening mediated by Sun2 suppression delays mechanical stress-induced cellular senescence. *Cell Death Discov* **9**, 167 (2023).

78. Jiao, S. *et al.* SUN1/2 controls macrophage polarization via modulating nuclear size and stiffness. *Nat Commun* **14**, 6416 (2023).

79. Krshnan, L. *et al.* Regulated degradation of the inner nuclear membrane protein SUN2 maintains nuclear envelope architecture and function. *Elife* **11**, e81573 (2022).

80. Cruz-Palomar, K. *et al.* SUN2 Modulates the Propagation of HSV-1. *J Virol* **96**, e0045322 (2022).

81. Xiang, Y. *et al.* Cofilin 1-mediated biphasic F-actin dynamics of neuronal cells affect herpes simplex virus 1 infection and replication. *J Virol* **86**, 8440–8451 (2012).

82. Datta, S., Snow, C. J. & Paschal, B. M. A pathway linking oxidative stress and the Ran GTPase system in progeria. *Mol Biol Cell* **25**, 1202–1215 (2014).

83. Danielsson, B. E. *et al.* Progerin-expressing endothelial cells are unable to adapt to shear stress. *Biophys J* **121**, 620–628 (2022).

84. Everett, R. D., Sourvinos, G. & Orr, A. Recruitment of herpes simplex virus type 1 transcriptional regulatory protein ICP4 into foci juxtaposed to ND10 in live, infected cells. *J Virol* **77**, 3680–3689 (2003).

85. Sandbaumhüter, M. *et al.* Cytosolic herpes simplex virus capsids not only require binding inner tegument protein pUL36 but also pUL37 for active transport prior to secondary envelopment. *Cell Microbiol* **15**, 248–269 (2013).

86. Ivanova, L. *et al.* Conserved Tryptophan Motifs in the Large Tegument Protein pUL36 Are Required for Efficient Secondary Envelopment of Herpes Simplex Virus Capsids. *J Virol* **90**, 5368–5383 (2016).

87. Buch, A. *et al.* Inner tegument proteins of Herpes Simplex Virus are sufficient for intracellular capsid motility in neurons but not for axonal targeting. *PLoS Pathog* **13**, e1006813 (2017).

88. Loconte, V. *et al.* Using soft X-ray tomography for rapid whole-cell quantitative imaging of SARS-CoV-2-infected cells. *Cell Rep Methods* **1**, 100117 (2021).

89. Chen, J.-H. *et al.* A protocol for full-rotation soft X-ray tomography of single cells. *STAR Protoc* **3**, 101176 (2022).

90. Parkinson, D. Y., Knoechel, C., Yang, C., Larabell, C. A. & Le Gros, M. A. Automatic alignment and reconstruction of images for soft X-ray tomography. *J Struct Biol* **177**, 259–266 (2012).

91. Belevich, I., Joensuu, M., Kumar, D., Vihinen, H. & Jokitalo, E. Microscopy Image Browser: A Platform for Segmentation and Analysis of Multidimensional Datasets. *PLoS Biol* **14**, e1002340 (2016).

92. Li, C. H. & Lee, C. K. Minimum cross entropy thresholding. *Pattern Recognition* **26**, 617–625 (1993).

93. Ahrens, J. P., Geveci, B. & Law, C. ParaView: An end-user tool for large-data visualization. in *Visualization Handbook* 717–731 (Unknown Publisher, 2005). doi:10.1016/B978-012387582-2/50038-1.

SUPPLEMENTARY MATERIAL

Supplementary Figures

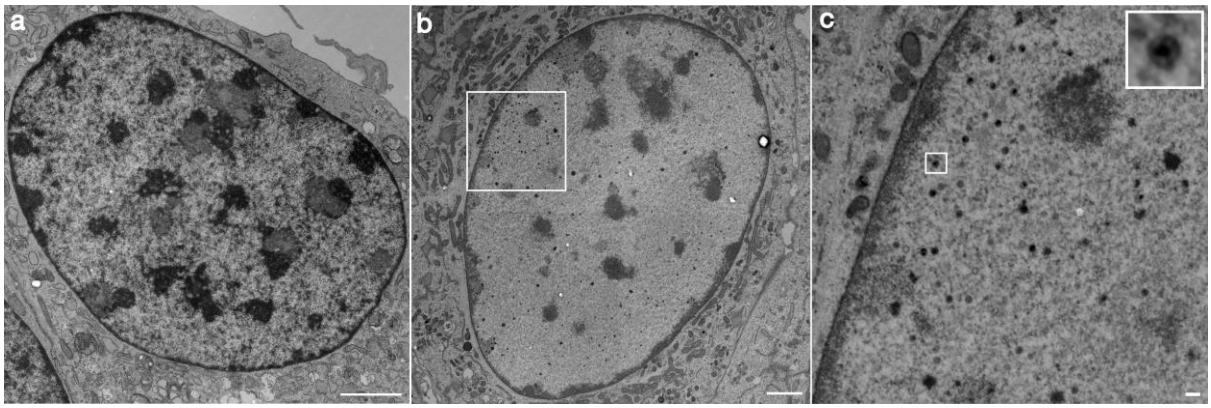

Figure S1. Distribution of nuclear chromatin and viral DNA in full capsids. Representative cross-section electron micrographs of (**a**) a noninfected and (**b**) an infected MEF cell at 8 hpi. ChromEM labeling was used to enhance the contrast on DNA. (**c**) The full viral capsids with DNA staining are shown. White squares show the magnified nucleoplasm and a full capsid. Scale bars, 2 µm (a, b) and 0.2 µm (c).

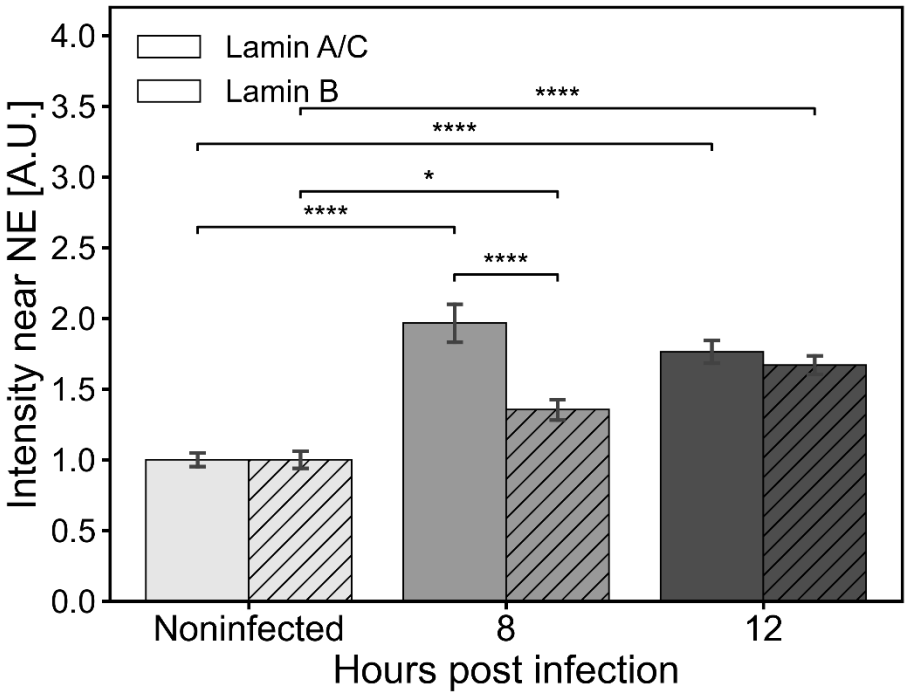

Figure S2. Normalized fluorescence intensity of lamin A/C and B in the nuclei of noninfected and infected cells at 8 and 12 hpi (n=74, 62 and 54, respectively). Statistical significance was determined using Tukey's test. The significance values shown are denoted as **** ($p<0.0001$) or * ($p<0.05$). Nonsignificant differences ($p \geq 0.05$) are not labeled.

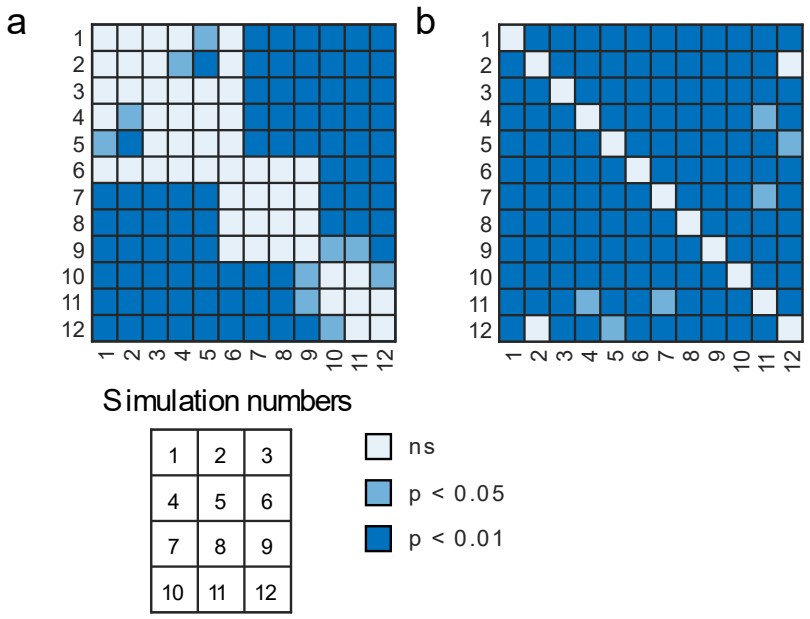

Figure S3. Statistical significances between simulations. Simulation case numbers and statistical significances between simulations presented in Fig. 6 for (**a**) Young's moduli (6f) and (**b**) nuclear envelope membrane tension (6g). Statistical significances were determined using the Games-Howell test. The significance values shown are denoted as p<0.001, p<0.01, p<0.05, or ns (not significant).

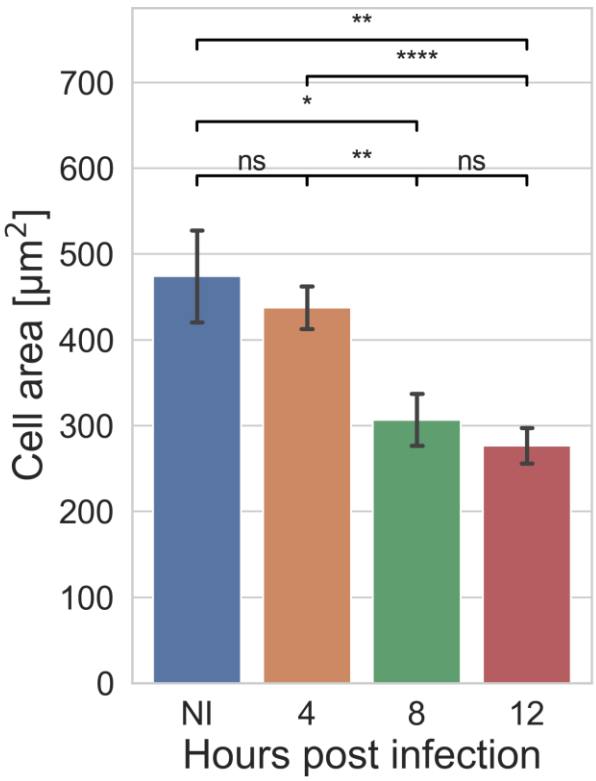

Figure S4. The cell contact area reduces as the infection proceeds. (**a)** Representative confocal images showing the cellular localization of actin in noninfected and HSV-1 ICP4-EYFP infected Vero cells at 12 hpi. The cells were immunolabeled with beta-actin (green) antibody and DNA was labeled with DAPI (blue). Scale bars, x µm. (**b**) The measurement of the area covered by the cells in noninfected and infected cells at 4, 8, and 12 hpi (n = x, y, z, q, respectively). The error bars show the standard error of the mean. Statistical significance was determined using Tukey´s test. The significance values shown are denoted as **** ($p<0.0001$), ** ($p<0.01$), * ($p<0.05$), or ns (not significant).

Supplementary Movies

Supplementary Movie 1. AFM analysis of nuclear stiffness.

Animation of AFM imaging of infected Vero cells at 4 hpi (left). Retraction curves of four measurements showing the force (deflection) versus cell height in living cells, retraction (cyan) and extension (blue) curves, and contact points (arrows) are shown (right). The vertical red line shows the progression of the measurement.

Supplementary Movie 2. Infection-induced changes of the nucleus.

Animation of cryo-soft X-ray (SXT) tomography imaging data of noninfected (NI) and infected MEF cells at 8 hpi. The high- (blue) and low-density chromatin (yellow), and viral replication compartment (VRC, green) are shown.

Supplementary Movie 3. Chromatin organization in the nuclear periphery is altered in infection.

Animation of focused ion-beam scanning electron microscopy (FIB-SEM) imaging data of noninfected and infected MEF cells at 8 hpi. The color bar indicates the high and low chromatin densities (yellow-green) and high and low thickness (yellow-blue). The nuclear envelope (cyan) and viral capsids (grey) are shown.

Supplementary Movie 4. Remodeling of nuclear organization during the growth of viral replication compartment.

Expansion of VRC as infection proceeds. The chromatin is shown in blue, VRC in green, lamina-associated domains (LADs) of the chromatin and chromatin crosslinks in cyan, and the NE in grey. The VRC located in the central region of the nucleus is not shown.

Supplementary Movie 5. AFM analysis of the infected cell.

AFM measurement of the nuclear stiffness of an infected cell. The effect of the colloidal probe of the cantilever (white) over the nucleus is presented. The cell membrane and cytoplasm are not presented. The chromatin is shown in blue, the lamina-associated domains (LADs) of the chromatin and chromatin crosslinks in green, and the NE in (grey). The VRC located in the central region of the nucleus is not shown.

Supplementary Tables

Supplementary Table 1. The transcription of nuclear lamins and lamin-associated proteins is regulated in response to viral infection.

The table presents the results of GRO-seq analysis showing upregulated (green-blue) or downregulated (red-orange) lamins and lamin-associated protein genes in infected Vero cells at 4 and 8 hpi.